Article

Three-Dimensional Nanoporous CNT@Mn$_3$O$_4$ Hybrid Anode: High Pseudocapacitive Contribution and Superior Lithium Storage

Wei Zou [1], Hua Fang [1,2,3,*], Tengbo Ma [4,*], Yanhui Zhao [5], Lixia Wang [1], Xiaodong Jia [1] and Linsen Zhang [1,2,3]

[1] College of Material and Chemical Engineering, Zhengzhou University of Light Industry, Zhengzhou 450002, China; 410418512@qq.com (W.Z.); 2014050@zzuli.edu.cn (L.W.); xdjia2017@zzuli.edu.cn (X.J.); hnlinsenzhang@163.com (L.Z.)
[2] Ceramic Materials Research Center, Zhengzhou University of Light Industry, Zhengzhou 450002, China
[3] Zhengzhou Key Laboratory of Green Batteries, Zhengzhou 450002, China
[4] Institute of Nuclear, Biological, and Chemical Defiance, PLA Army, Beijing 102205, China
[5] Luohe Letone Hydraulic Technology Co., Ltd., Luohe 462300, China; zyh@letone.cn
* Correspondence: fh@zzuli.edu.cn (H.F.); mtb1988@163.com (T.M.)

Abstract: A composite electrode of carbon nanotube CNT@Mn$_3$O$_4$ nanocable was successfully synthesized via direct electrophoretic deposition onto a copper foil, followed by calcination. By uniformly depositing Mn$_3$O$_4$ nanoparticles on CNTs, a nanocable structure of CNT@Mn$_3$O$_4$ can be formed, where the CNT acts as a "highway" for electrons and ions to facilitate fast transportation. Moreover, capacitive energy storage processes play a crucial role in lithium (Li) storage, especially during high scan rates. The significant contribution of capacitance is highly advantageous for the rapid transfer of Li$^+$ ions, which ultimately results in an improved reversible capacity and prolonged cycle stability of the battery. A high specific capacity of 1367 mAh g^{-1} was maintained over 300 charge–discharge cycles at a current density of 1 A g^{-1}, indicating excellent capacity retention and an extended cycle life. Furthermore, the synthesis process was facile and cost-effective, obviating the need for complex procedures such as mixing and pasting. Additionally, no binder was required, thereby enhancing battery quality efficiency.

Keywords: Mn$_3$O$_4$; carbon nanotubes; electrophoretic deposition; lithium-ion batteries; anode material

1. Introduction

As the world confronts environmental challenges stemming from fossil fuel combustion, it is imperative that governments and scientists expeditiously explore and cultivate green renewable energy sources. Solar and wind energy are two examples of such sources; however, their intermittent nature and instability pose a threat to the security of power systems when used in large quantities. Hence, it is crucial we expand highly efficient energy conversion and energy storage systems for power produced by sustainable sources like solar, wind, and tidal energy to ensure a sustainable and secure energy future [1].

Rechargeable batteries, particularly lithium-ion batteries (LIBs), have made significant strides in the energy storage sector and renewable power technology in recent years. LIBs possess high energy density, a prolonged cycle life, and eco-friendliness, rendering them a promising option for clean energy storage systems in portable electronics, electric vehicles (EVs), and wind/solar power devices [2,3]. The speedy progress of portable consumer electronics and electric vehicles has created a critical requirement for next-generation LIBs with even higher energy density. Currently, carbonaceous materials, particularly graphite, are widely utilized as low-cost anode materials in commercial lithium-ion batteries due to their low working potential and lengthy longevity [1]. However, the graphite material currently available on the market has already reached its theoretical capacity of

372 mAh g^{-1} and is approaching its limit [2]. Hence, the quest for high-energy-density anode materials in LIBs is becoming increasingly pressing.

Transition-metal oxide compounds, such as MxOy (where M represents Ni, Mn, Co, Fe, and other elements), possess high theoretical energy density and have been identified as promising anode materials for lithium-ion batteries [3–5]. Mn_3O_4 is considered a highly attractive anode material option for LIBs due to its abundant and eco-friendly nature, as well as its significant theoretical capacity of 936 mAh g^{-1} [6]. Since the first report on Mn_3O_4 as a host for electrochemical Li insertion by Goodenough's team, Mn_3O_4 has drawn considerable focus as a qualified candidate for anode in LIBs. Nonetheless, Mn_3O_4 experiences significant expansion in volume during lithiation and delithiation processes, resulting in suboptimal cycle stability [7]. Furthermore, the low electron conductivity of Mn_3O_4 (10^{-7} to 10^{-8} S cm^{-1}) impedes its application as an anode for LIBs, resulting in an inadequate rate capability [8,9].

To address the challenges mentioned above, researchers have adopted two widely used strategies, namely the creation and production of nanocomposite materials containing a conductive matrix. The structural stability of nanoscale active materials is bolstered by the reduced mechanical stress within particles and smaller variations in volume, as has been demonstrated [5]. Additionally, the nanoscale electrode–electrolyte interface provides an increased contact area, thereby enhancing kinetic properties and reducing the Li$^+$ ion transfer pathway [3]. On the other hand, the use of conductive matrix materials including porous carbon, CNT, graphene, or conducting polymer can significantly improve electron conductivity and cushion large volume fluctuation, leading to improved rate performance and cycle stability [4]. Anchoring ultrafine Mn_3O_4 nanoparticles on a highly conductive carbon matrix can be an effective way to achieve an outstanding specific capacity, exceptional rate capability, and extended cycle life. Several studies have aimed to develop nanocomposites incorporating Mn_3O_4 nanoparticles, including the ultrasound-assisted in situ growth of Mn_3O_4 nanoplates anchored on rGO [6]. After 40 cycles of charging and discharging at 0.1 A g^{-1}, the specific capacity demonstrated was 1400 mAh g^{-1}. Several studies have reported on the development of Mn_3O_4-based nanocomposites with an improved specific capacity. For instance, Varghese et al. designed a Mn_3O_4-rGO nanocomposite via hydrothermal synthesis, which exhibited a reversible capacity of 474 mAh g^{-1} when subjected to 100 mA g^{-1} cycling [10]. A mesoporous Mn_3O_4/C nanocomposite was directly synthesized via thermolysis by Peng et al., demonstrating a high capacity of 1032 mAh g^{-1} when cycled at 200 mA g^{-1} [11]. Gangaraju reported a graphene–carbon nanotube (CNT)-Mn_3O_4 composite developed using a microwave technique; cycling the material at 1 A g^{-1} for 300 cycles resulted in a high capacity of 1337 mAh g^{-1} [12]. However, some carbon-based nanocomposites display weak interaction between Mn_3O_4 nanoparticles and the conductive carbon matrix, resulting in capacity degradation during long charge–discharge tests.

Since Taberna's initial report on the use of nanostructured current collectors in high-power electrochemical energy storage, scientists have been exploring the application of three-dimensional nanoporous electrodes to tackle issues such as pulverization and capacity degradation [13]. In this study, a three-dimensional (3D) nanoporous hybrid electrode was synthesized by the researchers using a simple electrochemical method. The 3D nanoporous electrode is composed of a CNT@Mn_3O_4 core–sheath nanocable structure, where Mn_3O_4 nanoparticles are uniformly anchored onto an interconnected matrix of carbon nanotubes. The 3D nanoporous electrode exhibits a remarkable performance as an LIB anode, being characterized by a high specific capacity, exceptional rate capability, and extended cycle stability. After undergoing 300 cycles of charge and discharge at a rate of 1 A g^{-1}, the electrode maintained an impressive specific capacity of 1367 mAh g^{-1}. Electrochemical kinetic analysis indicated that the significant contribution of pseudocapacitance had a positive impact on its superior lithium storage performance.

2. Experimental Details

2.1. Synthesis of CNT@Mn₃O₄ Hybrid Electrode

The reagents utilized in the experiments were of exceptional purity, adhering to specifications for analytical grade. The carbon nanotubes (CNTs) were obtained from Chengdu Organic Chemical Company in Chengdu, China. They had an outer diameter of approximately 50 nm and a length ranging from 0.5 to 2 μm. After undergoing refluxing in concentrated nitric acid for 6 h, the CNTs were ready for use.

A facile electrochemical synthesis strategy, which combines electrophoretic deposition with electrochemical deposition, was used to deposit a three-dimensional nanoporous CNT@Mn₃O₄ hybrid electrode on a commercial copper foil. The deposition suspension was prepared by ultrasonically dispersing 13 mg of pretreated CNTs and 120 mg $Mn(NO_3)_2$ (50% aqueous solution, AR) in 100 mL of absolute ethanol. A rectangular copper foil measuring 30 mm by 40 mm was utilized as the cathode, while a rectangular platinum foil of the same size served as the anode. The copper cathode and platinum anode were positioned parallel to each other with a 10 mm gap between them in the mixture. The deposition process was conducted for a duration of 300 s under a constant voltage of 50 volts. In this deposition process, the electrophoretic deposition of CNT and cathodic deposition of Mn^{2+} ions occurred synchronously, resulting in the one-step formation of a hybrid electrode. A diagram of the specific synthesis steps can be found in Figure S1 of the Supplementary Information. After deposition, the as-obtained hybrid electrode was initially rinsed with ethanol to eliminate residual $Mn(NO_3)_2$. Subsequently, the CNT@Mn₃O₄ hybrid electrode was obtained via calcination in a N_2 environment at 300 °C for 3 h. Photos of the as-prepared CNT@Mn₃O₄ sample deposited on copper foil can be found in Figure S2 of the Supplementary Information.

2.2. Material Characterization

The structure was examined using a field-emission scanning electron microscope (SEM, JSM-7001F) and transmission electron microscopy (TEM, JEOL 2010F). The crystallographic arrangement of CNT@Mn₃O₄ was identified using X-ray diffraction (XRD, Rigaku D/Max-2400). The nitrogen adsorption–desorption test at 77 K (BELSORP-Mini II) was employed to characterize the pore size distribution and specific surface area [14].

2.3. Electrochemical Characterization

The CNT@Mn₃O₄ was utilized as the active electrode and machined into a circular shape with a 14 mm diameter by means of a cutting machine. Subsequently, a CR2016-type coin cell was fabricated in a vacuum glove box (MB-10-G, MBRAUN) featuring a H_2O and O_2 content below 1 ppm. The electrolyte utilized in the experiment was a 1 M $LiPF_6$ solution dissolved in a 1:1 (*v*/*v*) blend of ethylene carbonate (EC) and dimethyl carbonate (DMC). The cell was composed of a Celgard 2300 membrane separator, with lithium foil serving as both the reference and counter electrodes.

The coin cell was subjected to galvanostatic charge–discharge (GCD) tests using a Neware battery test system. The experiments were conducted across a range of current densities spanning from 0.1 to 10 A g^{-1} and under a voltage range of 0.01 to 3 V (vs. Li/Li$^+$) in order to obtain comprehensive data. Furthermore, cyclic voltammetry (CV) experiments were performed using an electrochemical workstation (CHI660E) with a fixed voltage range of 0.01 to 3 V (vs. Li/Li$^+$). Electrochemical impedance spectroscopy (EIS) tests were conducted using a voltage amplitude of 10 mV and a frequency range spanning 10^5 to 0.01 Hz. The loading of active material in the electrode film we prepared was determined to be 0.358 mg.

3. Results and Discussion

3.1. Microstructural Studies

The morphology was examined via SEM and TEM analysis, as depicted in Figure 1. As shown in Figure 1a, the CNTs were coated with Mn₃O₄ particles, resulting in a

CNT@Mn_3O_4 nanocable with a rough surface and a consistent diameter of approximately 110 nm. The TEM images presented in Figure 1b,c demonstrate the anchoring of Mn_3O_4 nanocrystals onto the sidewall of the CNTs. As depicted in Figure 1d, the observed lattice spacings of 2.78 Å and 3.36 Å correspond to the interplanar spacing of the (103) plane of Mn_3O_4 (PDF card number 24-734) [15] and the (002) plane of CNTs (PDF card number 26-1079) [5], respectively. The Mn_3O_4 coating sheath layer had a thickness of approximately 13 nm. This nanocable structure facilitates the transport of electrons.
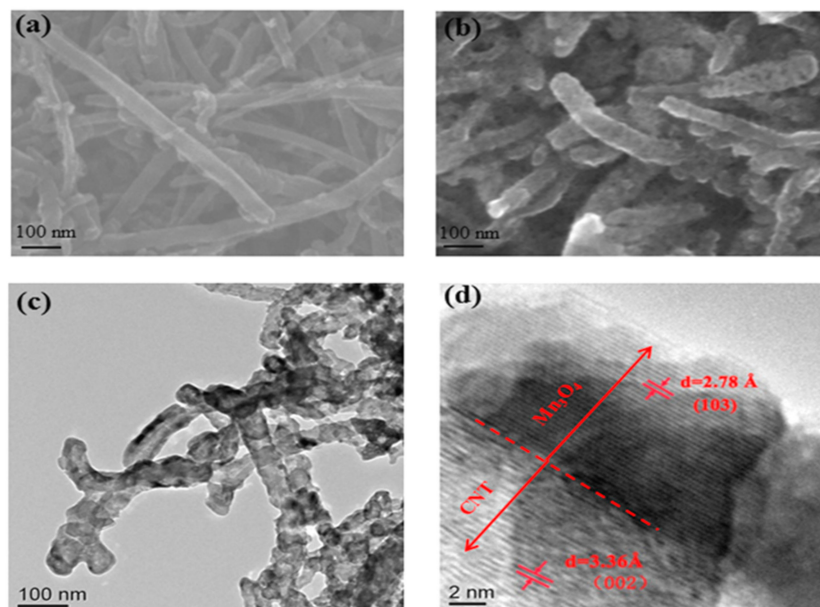

Figure 1. (**a**) SEM images of CNT; (**b**) SEM images of CNT@Mn_3O_4; (**c**,**d**) TEM images of CNT@Mn_3O_4 nanocable.

The XRD spectrum of the nanocable in Figure 2 reveals that Mn_3O_4 (PDF24-734) was the predominant crystalline phase, as evidenced by most of the observed diffraction peaks. Additionally, the diffraction peak at $2\theta = 26.4°$ can be attributed to the (002) crystallographic plane of the hexagonal carbon structure in CNTs (PDF26-1079). The relatively broad peaks observed at the (211), (103), and (101) planes of Mn_3O_4 suggest that the sheath was composed of nanoparticles. Applying Scherrer's formula, $D = n \cdot \lambda / (\beta \cdot \cos \theta)$, we calculated a mean crystal size of ~20 nm for Mn_3O_4 [16].
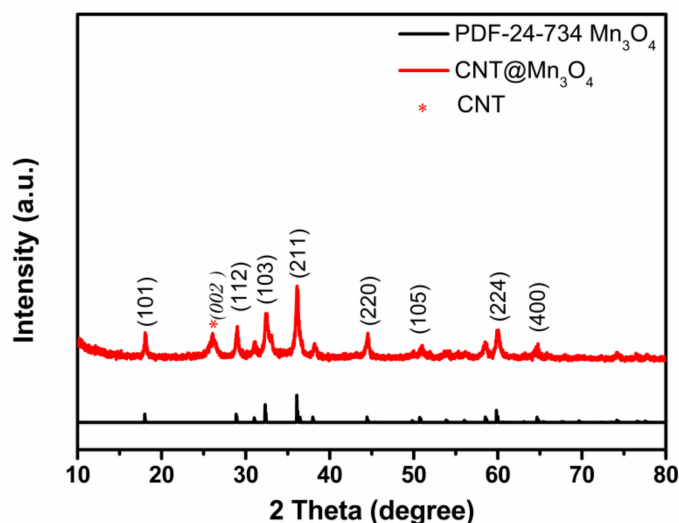

Figure 2. XRD patterns of CNT@Mn_3O_4 nanocable.

The N_2 sorption isotherm depicted in Figure 3a exhibits a type IV isotherm with a hysteresis loop, indicating the presence of mesopores [15,17]. The CNT@Mn_3O_4 material demonstrated a remarkable specific surface area of 75.477 m^2 g^{-1}, a total pore volume of 0.1805 cm^3 g^{-1}, and an average pore size of 11.711 nm. The pore size distribution curve exhibited two distinct peaks: one at approximately 2 nm indicating the presence of micropores and another broader peak above 10 nm corresponding to mesopores. The high surface area and the hierarchical pore distribution facilitate rapid migration of lithium ions, shorten solid diffusion length, and buffer volume expansion during ion insertion into the active material. Consequently, this material can provide improved power performance as an LIB anode.
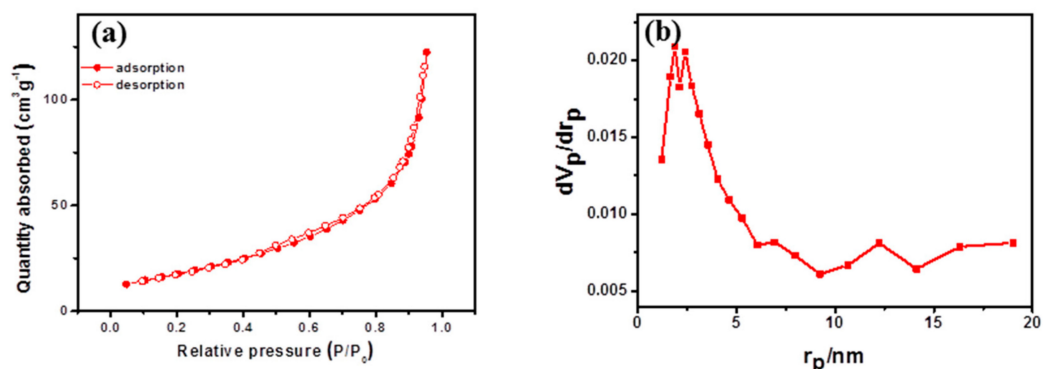

Figure 3. (**a**) N_2 sorption isotherm diagram; (**b**) pore size distribution.

3.2. Electrochemical Studies

The electrochemical behavior was initially evaluated via cyclic voltammetry (CV). Figure 4 illustrates the CV profile of the CNT@Mn_3O_4 electrode, depicting the current variation as a function of applied potential within the voltage range of 0.01 to 3.0 V vs. Li/Li^+ at a scan rate of 10 mV s^{-1}. A broad cathodic peak at ~1.3 V was observed in the first stage due to the reduction of Mn^{3+} to Mn^{2+} [18,19]. The cathodic peaks observed at 0.02 V during the first scan were attributed to the process of inserting Li^+ into the CNT framework. The reduction characteristic observed at 0.4 V corresponds to the reduction of Mn(III) to Mn(0). Regarding the anodic branch, the broad peaks observed at 1.3 V are associated with Mn(II) oxidation to Mn(III), while the other peak corresponds to metallic Mn oxidation to Mn(II). In subsequent cycles, a solid–solid interface formation caused the broad reduction peak at ~1.3 V to shift towards 1.4 V. The voltage of the 0.4 V peaks underwent a downward shift to 0.3 V, which is a characteristic feature of manganese oxide electrodes and indicates structural rearrangements associated with lithium insertion during the initial cycle [20,21]. The absence of any noticeable variation between the second and subsequent cycles, coupled with the excellent cycling stability observed, is indicative of the material's high reversibility for lithium storage [10,22]. This underscores its electrochemical reaction mechanism.
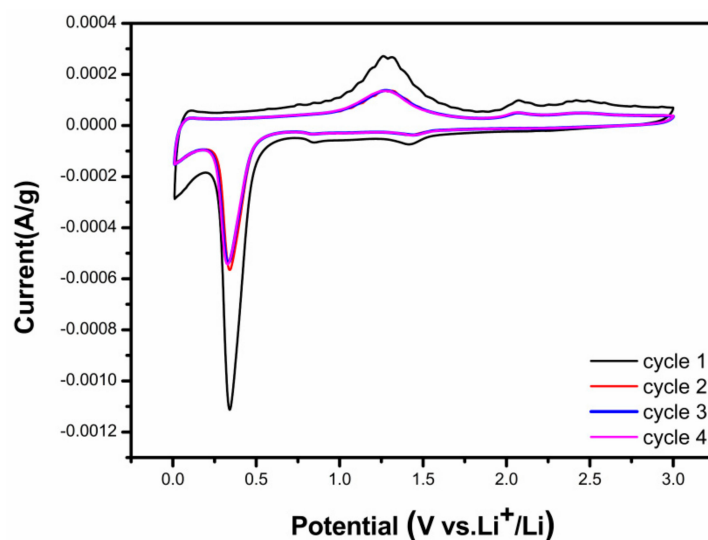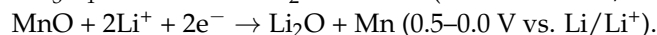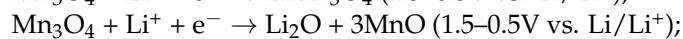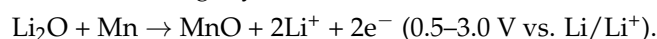
Figure 4. CV curves of the CNT@Mn$_3$O$_4$ nanocable at 10 mV s^{-1}.

Initial discharge cycle:

Mn$_3$O$_4$ + Li$^+$ + e$^-$ → LiMn$_3$O$_4$ (1.5–0.5V vs. Li/Li$^+$);
Mn$_3$O$_4$ + Li$^+$ + e$^-$ → Li$_2$O + 3MnO (1.5–0.5V vs. Li/Li$^+$);
MnO + 2Li$^+$ + 2e$^-$ → Li$_2$O + Mn (0.5–0.0 V vs. Li/Li$^+$).

Initial charge cycle:

Li$_2$O + Mn → MnO + 2Li$^+$ + 2e$^-$ (0.5–3.0 V vs. Li/Li$^+$).

Another criterion for assessing the performance of electrode materials is their rate capability under various applied currents. As depicted in Figure 5a, the component exhibited a high capacity of 869 mAh g^{-1} at a current density of 0.1 A g^{-1} and maintained a relatively impressive capacity of 309 mAh g^{-1} even when the current density was increased to 10 A g^{-1}, which is highly comparable to previously reported values [23–25]. Upon returning to a current-specific mass of 0.1 A g^{-1}, the ingredient demonstrated exceptional reversibility with a capacity retention of 900 mAh g^{-1}, indicating its superior rate performance and cycle stability.
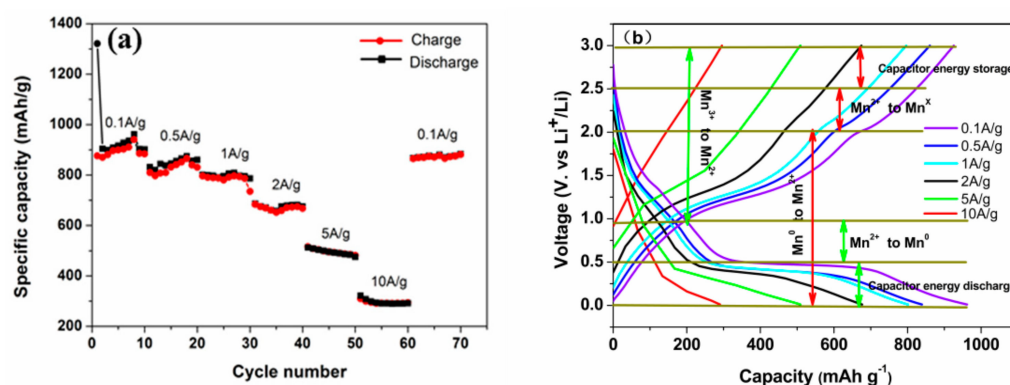

Figure 5. (**a**) Rate performance of the CNT@Mn$_3$O$_4$ nanocable; (**b**) charge–discharge curves of the CNT@Mn$_3$O$_4$ nanocable under varying current loads.

Figure 5b shows the galvanostatic charge–discharge (GCD) plots at different electric current densities. A slight variation in the polarization voltage of the electrode material was observed with an increase in current density, indicating that the electrode material has high electron and ion conductivity. The high conductivity is attributed to the unique nanocable structure, whereby CNTs provide rapid electron transport and the 3D nanoporous morphology facilitates efficient ion transportation [26,27]. Simultaneously, it served as a structural

support to mitigate the volume expansion and exhibited capacitive behavior in the form of linear platforms with negative slopes ranging from 0 to 0.5 V, which may be attributed to lithium storage at the interface [14].

The stable voltage plateau observed at 0.5 V is attributed to the Faradaic involvement of the Li$^+$ insertion mechanism. As current density increases, this platform becomes slightly shorter and eventually disappears at current densities greater than 5 A g^{-1}. The sluggish reaction kinetics of the Mn$_3$O$_4$ sheath are primarily responsible for this phenomenon [28]. Encouragingly, no significant capacity reduction was observed below 0.5 V due to the capacitive nature of interfacial lithium storage. As is well known, capacitive behavior is characterized by a high rate capability, which can be attributed to the interfacial lithium storage mechanism described above.

Simultaneously, the discharge platform of capacitor performance prevails, aligning with the high current charge and discharge characteristics of capacitor energy storage. This capacitance contribution greatly facilitates rapid transmission of Li$^+$, resulting in exceptional reversible capacity and long-cycle stability [9]. This observation offers further insight into the outstanding high rate performance of these materials.

The cycling performance of the CNT@Mn$_3$O$_4$ electrode was assessed by carrying out galvanostatic charge–discharge (GCD) experiments at a current density of 1 A g^{-1}. As depicted in Figure 6a, the coulombic efficiency exhibited a sharp rise to approximately 98% and remained stable throughout subsequent cycles, which can be attributed to the enhanced reversibility of CNT@Mn$_3$O$_4$. From cycles 2 to 60, the specific capacity of the battery decreased from 768 to 511 mAh g^{-1}, but then consistently increased and reached 1389 mAh g^{-1} in the later cycles. It is not uncommon for previous studies to report an increase in capacity [29,30]. The primary potential factors contributing to this phenomenon were as follows. (1) Electrochemical grinding is caused by repeated volume expansion and the lithiation–delithiation process can result in contraction of the electroactive material. This leads to an increase in contact area between the active site and the electrolyte. (2) Lithium storage at the two-phase interface between metal and Li$_2$O can be achieved [13]. (3) The reversible formation and dissolution of the solid electrolyte interphase (SEI) layer enables lithium storage [31]. (4) The CNT substrate served as a scaffold to mitigate the volume fluctuations that occur during charge and discharge cycles, ensuring capacity stability [32–34]. (5) The robust architecture of the hybrid nanomembranes [35]. The TEM images of the CNT@Mn$_3$O$_4$ materials after different cycles in Figure 6b–d provide evidence to support these conclusions. In particular, Figure 6b,c demonstrate that Mn$_3$O$_4$ nanoparticles are uniformly distributed on the CNT scaffold, resulting in a highly porous three-dimensional structure. As the lithiation–delithiation cycle progressed, as shown in Figure 6d, the active material underwent increased porosity and loosening, thereby enhancing the number of active sites associated with electrochemical reactions and resulting in an optimal lithium storage capacity for the composite.

The CV splines of CNT@Mn$_3$O$_4$ were tested at a scan rate of 10 mV s^{-1} after different cycles. At the 60th cycle, the capacity reduced its minimum and then began to increase. After 60 iterations, the format of the CV document remained consistent with the output preceding the loop. After 200 and 300 cycles, the reduction peak at 0.02 V and oxidation peak at 2.1 V were significantly intensified, which can be attributed to the reaction progression and increased electrochemical grinding effect on the lithium storage interface, resulting in an increase in capacity. For more comprehensive information, please refer to the relevant figures and explanations provided in Figure 6. Furthermore, it should be noted that the length of the discharge–charge platform depicted in Figure 7b increases proportionally with the number of cycles, thus providing additional evidence to support this conclusion.
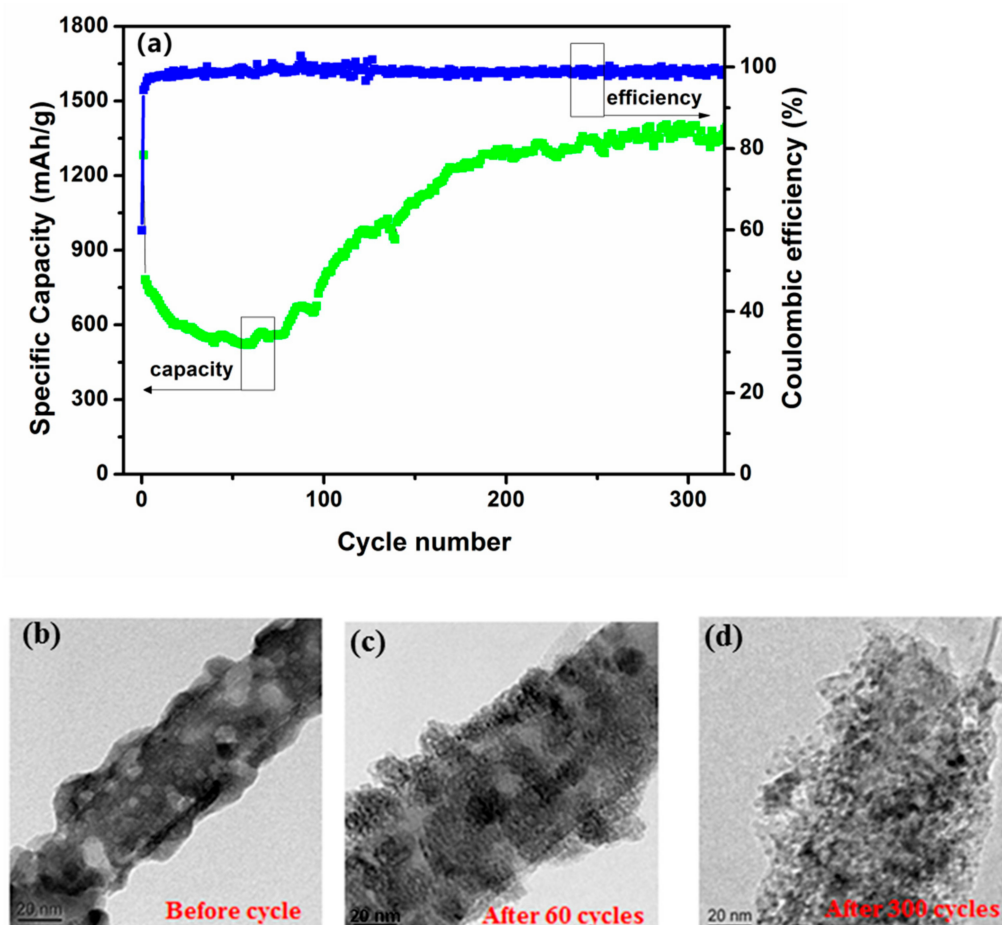
Figure 6. (**a**) The cycling stability of the CNT@Mn$_3$O$_4$ nanocable as anodes for LIBs at a current density of 1 A g^{-1}; (**b**) TEM images of the CNT@Mn$_3$O$_4$ nanocable before cycling; (**c**) after 60 cycles; (**d**) after 300 cycles.
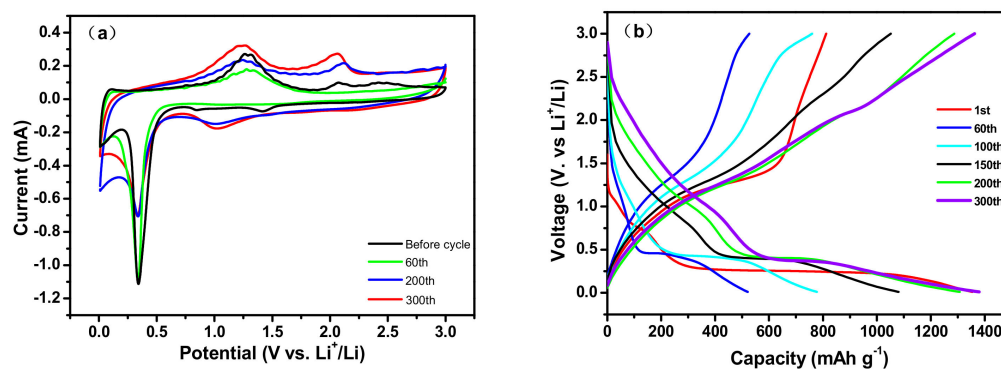

Figure 7. (**a**) CV splines of the CNT@Mn$_3$O$_4$ nanocable at 10 mV s^{-1} after different cycles; (**b**) charge–discharge curves of the CNT@Mn$_3$O$_4$ nanocable at a current density of 1 A g^{-1}.

The electrochemical performance of the CNT@Mn$_3$O$_4$ nanocable material for lithium-ion storage was evaluated using a GCD approach. Figure 7b illustrates the discharge–charge profiles of the CNT@Mn$_3$O$_4$ nanocable material at a current density of 1 A g^{-1} within the voltage range of 0.01 to 3 V (vs. Li/Li$^+$) over multiple cycles. During the initial cycle, the CNT@Mn$_3$O$_4$ nanocable material exhibited a discharge capacity of 814 mAh g^{-1} and a charge capacity of 1307 mAh g^{-1}. The primary irreversible capacity loss occurred during the formation of a solid electrolyte interphase (SEI) layer, which arose from the decomposition of the electrolyte. In the sixtieth cycle, the coulombic efficiency of the specimen

increased to 98%; however, its capacity reached a nadir due to inadequate wettability at the interface between electrolyte and active material. As charging and discharging proceeded, capacity gradually recovered. After three hundred revolutions, a charging capacity of 1386 mAh g^{-1} and a discharging capacity of 1367 mAh g^{-1} were achieved due to the secondary activation and electrochemical reaction, resulting in an impressive coulombic efficiency of approximately 98.6% [30,36]. The performances exhibited superior characteristics compared to those previously reported [4,31,33,37]. The charge and discharge voltage plateaus were observed at approximately 0.4 V, 1.3 V, and 2.1 V, respectively. These findings are consistent with the results obtained from the CV curves depicted in Figure 7a.

To further investigate the factors contributing to the superior efficacy of CNT@Mn$_3$O$_4$ as an electrode material for LIBs, cyclic voltammetry (CV) measurements were conducted with scan rates ranging from 0.2 to 1.2 mV s^{-1} to analyze the kinetics of the electrode. The position of the redox peak in the CV curve remained consistent across different scanning rates, indicating a stable electrochemical performance. The high electrochemical reversibility indicates the potential of electrode materials to store energy through both Faraday and non-Faraday process [28,38], which can be qualitatively examined using CV measurements obtained at various scan rates [39]:

$$i = av^b$$

where a and b represent Ka. The slope of the log (i) to log (v) curve can be utilized for calculating the b value, which characterizes the charge storage dynamics during the charge–discharge process. A b value of 0.5 indicates a Faraday process controlled by diffusion [9], whereas a b value of 1 signifies that the electrode is governed by capacitance behavior [40,41]. As depicted in Figure 8b, the b value of the cathodic peak at 0.4 V for the CNT @ Mn$_3$O$_4$ electrode was determined to be 0.65, while that of the anodic peak was calculated as 0.8. This equation suggests that the electrochemical reaction is primarily influenced by the interplay between the diffusion mechanism and the capacitive response. Furthermore, the current output at a specific potential can be separated into two components. One is diffusion-controlled partial current ($k_1 v^{1/2}$), as illustrated by the following equation [42]:

$$i\,(V) = k_1 v^{1/2} + k_2 v$$

Both k_1 and k_2 are variables that can be calculated based on the slope of the $i(V)/v^{1/2}$ and $v^{1/2}$ curves, respectively. The parameter k_2 serves as a discriminant for capacitive current ($k_2 v$) from the total current. Figure 8c illustrates that the CNT@Mn$_3$O$_4$ electrode contributes to a capacitance of 73.4% at a scanning speed of 1 mVs^{-1}. Figure 8d summarizes the capacitance contributions at different scan rates, which were found to be 46.0%, 58.0%, 67.3%, 70.6%, 73%, and 77% at scan rates of 0.2, 0.4, 0.6, 0.8, 1, and 1.2 mVs^{-1}, respectively. The graph depicted in Figure 8e illustrates that the CNT@Mn$_3$O$_4$ electrode's capacitance contribution reached a remarkable 89% after undergoing 300 cycles at a scan rate of 1 mV s^{-1}, indicating the predominant role played by the energy storage process in its capacity contribution [43,44]. There are two primary factors contributing to this observation. Firstly, the CNT@Mn$_3$O$_4$ electrode material exhibits a remarkably high specific surface area of 75.477 m^2 g^{-1} based on BET testing, which enhances surface adsorption and provides Faraday capacitance. Secondly, during cycling, Mn$_3$O$_4$ generates nanoscale LiO$_2$ and M, which create numerous interfaces. These interfaces provide capacitive interfacial lithium storage and significantly contribute to the overall capacitance of the electrode [14]. The analysis of electrochemical kinetic test data suggests that capacitive energy storage processes play a crucial role in lithium (li) storage, particularly at high scan rates. The significant contribution of capacitance is highly advantageous for the quick transfer of Li$^+$ ions, ultimately resulting in improved reversible capacity and prolonged cycle stability of the battery [14].
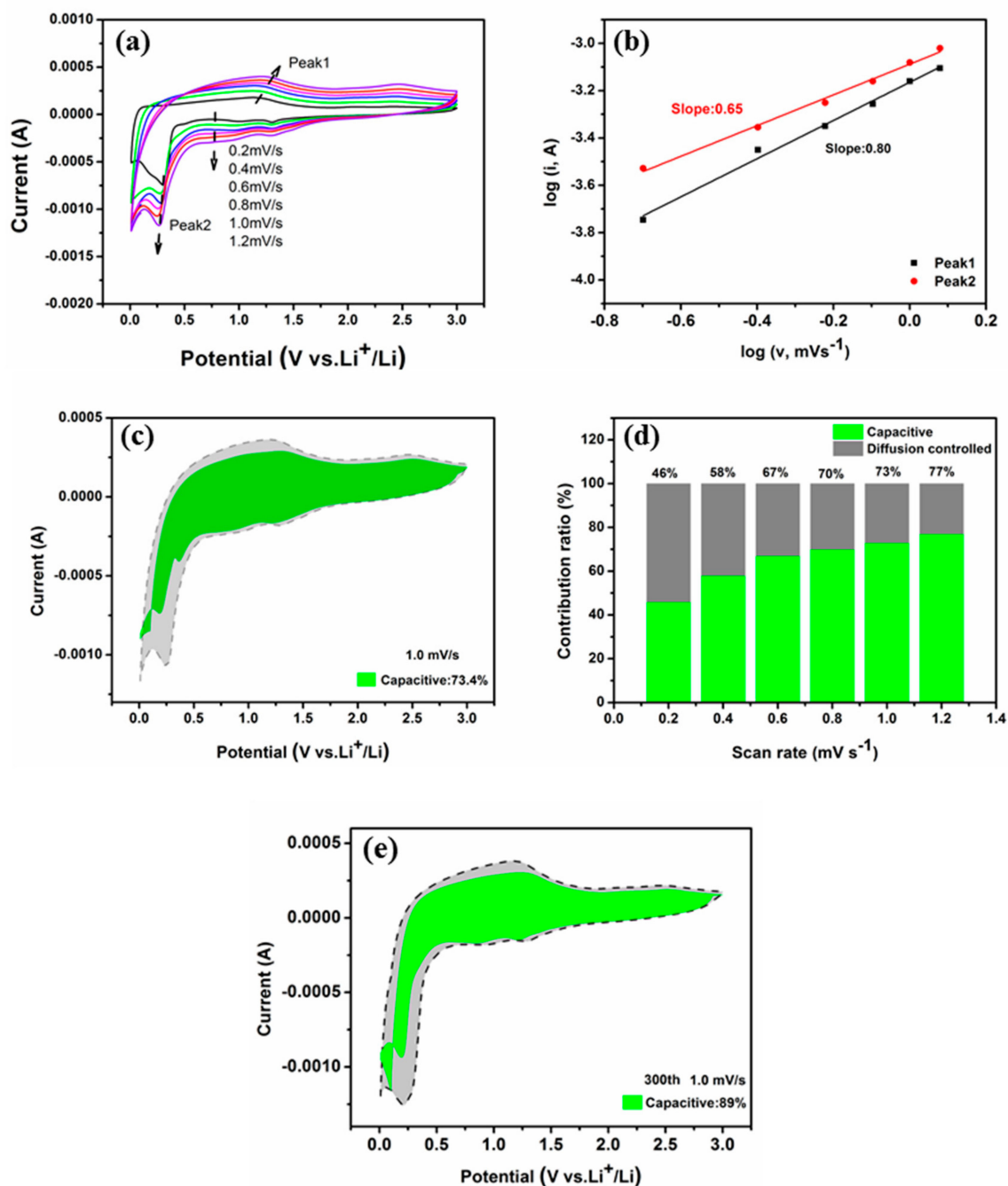
Figure 8. (**a**) CV curves with scan rates from 0.2 to 1.2 mV s^{-1}; (**b**) log i vs. log v plots at oxidation and reduction state; (**c**) capacitive contribution at 1 mV s^{-1}; (**d**) the capacitive capacity contribution at various scan rates; (**e**) capacitive contribution at 1 mV s^{-1} after 300 cycles.

The behavior of capacitive electrodes was analyzed using EIS. The Nyquist plots of CNT@Mn$_3$O$_4$ exhibited a partial semicircle and a straight sloping line, as depicted in Figure 9. The size of the semicircle in the diagram indicates the Faradic charge transfer resistance (Rct), which reflects the electrode's surface area and conductivity [31]. Alternatively, the diffusion of ions was correlated with the straight sloping line. In the high-frequency region, the intercept associated with electrolyte resistance (Rele) in the Nyquist plot increased over cycles, indicating enhanced lithium-ion penetration into the active component surface area during cycling. Moreover, the slope of the sloping line became steeper with cycling, indicating that CNT@Mn$_3$O$_4$ exhibited enhanced electrolyte ion diffusion during the redox reaction [31].
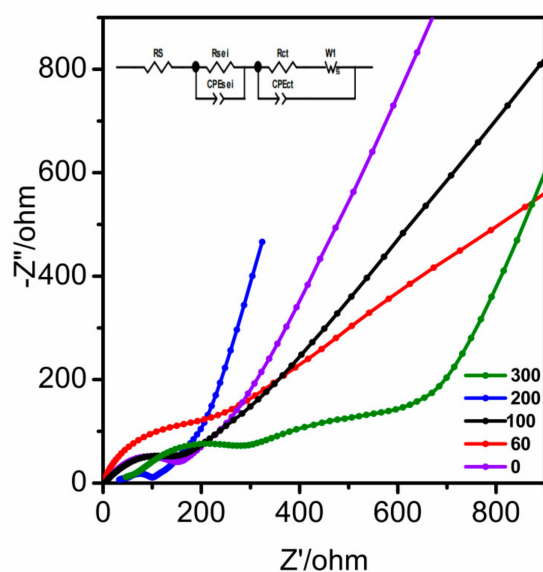
Figure 9. EIS of the CNT@Mn₃O₄ nanocable after different cycles.

The graded porous network structure of CNT@Mn₃O₄ facilitates the effective infiltration of the electrolyte into the pores of the electrode material, thereby mitigating polarization and augmenting its specific capacity. A lower Rct value was observed as a result of the graded porous network structure. However, after 300 cycles, there was a substantial increase in Rct, which was attributed to volume fluctuations in the electrode material, dissolution and aggregation of Mn₃O₄ nanoparticles, and transformation of the spinel Mn₃O₄ [45,46].

To gain a more comprehensive understanding of the electrochemical mechanism, the electrode's EIS was examined both before and after cycling. As depicted in Figure 9 by the purple line, the EIS prior to cycling displays an intersection point on the real axis at high frequency that represents electrolyte resistance—primarily caused by electrolyte and other battery components—which is ohmic in nature. The decay in the low-frequency range is indicative of the charge transfer resistance and the permanent phase element at the interface between the electrode and electrolyte. CPEct is associated with the electric double-layer capacitor, while W1 characterizes diffusion-related phenomena in the system, including the salts and lithium-ion diffusion into the active material [32,47]. The linear region at the low-frequency range depicts this phenomenon. After the 200 cycles, the EIS exhibited three distinct segments, each featuring an equivalent series resistance (R_s) in the high-frequency region. This parameter is closely related to the ohmic portion of electrode impedance and encompasses contributions from electron transport.

Several factors influence the behavior of an electrode, including its conductivity, the ionic conductivity of the electrolyte solution, and any electrical contact resistance associated with battery hardware, current collectors, or electrode materials. The arc in the mid-to high-frequency range represents the resistance (R_{SEI}) and capacitance (C_{SEI}) of the SEI layer, while the arc in the medium-frequency range corresponds to charge transfer resistance (R_{ct}) and a constant phase element at the electrode–electrolyte interface. The constant phase element (CPE) is associated with double-layer capacitance, whereas linear decay observed in the low-frequency region can be attributed to W, which represents lithium-ion diffusion through an electrode [32].

Based on the blue lines in Figure 9, the semicircle radius of the electrode was significantly reduced after cyclic activation, indicating a smaller Rs due to the presence of CNT@Mn₃O₄ nanostructures during cycling. The accumulation of CNTs hindered the aggregation of Mn₃O₄, resulting in increased interlayer spacing and a higher number of electroactive sites. This facilitates charge transport and electrolyte infiltration, as evidenced by the steeper slope and shorter line lengths in the low-frequency region after 200 cycles.

The lithium diffusion rate was accelerated, while the change in the diffusion path was minimized. These observations are consistent with those from TEM analysis shown in Figure 6, which indicate that the electrode became more porous and independent after cycling. Moreover, the nanostructures retained their original morphology, providing further evidence of their exceptional lithium storage performance.

4. Conclusions

In this study, the researchers employed the electrophoretic deposition technique to fabricate a CNT@Mn$_3$O$_4$ nanocable electrode material. This approach enabled direct deposition of active material onto commercially available copper foil, which can function as a current collector for LIBs. Moreover, the absence of a binder contributed to the enhanced quality and efficiency of the battery. The CNT@Mn$_3$O$_4$ material exhibited an impressive stable reversible capacity of 1335 mAh g^{-1} at a current density of 1 A g^{-1}, demonstrating exceptional cycling stability and rate performance. The unique 3D nanoporous architecture of this material enables effective absorption of large volume fluctuations and enhances the speed of electron transfer and transport of lithium ions during charging and discharging processes. Incorporating a porous carbon coating can effectively protect the active material from pulverization, while also enhancing cycling stability and enabling faster charging/discharging rates through increased electrical conductivity. Therefore, the CNT@Mn$_3$O$_4$ composite material exhibits great potential as a superior anode material for high-performance lithium-ion batteries. This study offers a novel perspective on synthesizing high-performance electrode materials using simple and cost-effective methods. The results of this study are expected to advance the development of rechargeable lithium-ion batteries with high power and a long cycle life for energy storage applications.

Author Contributions: Conceptualization, H.F. and W.Z.; methodology, H.F. and W.Z.; software, validation, formal analysis, and investigation, W.Z. and Y.Z.; resources, W.Z. and H.F.; data curation, W.Z. and H.F.; writing—original draft preparation, W.Z. and H.F.; writing—review and editing, H.F.; visualization, X.J. and L.W.; supervision, L.Z., T.M. and H.F.; project administration, H.F., T.M. and L.Z.; funding acquisition, H.F. and L.Z. All authors have read and agreed to the published version of the manuscript.

Data Availability Statement: Not applicable.

Conflicts of Interest: The authors declare no conflict of interest.

References

1. Zheng, S.; Dong, F.; Yue, P.; Han, P.; Yang, J. Research Progress on Nanostructured Metal Oxides as Anode Materials for Li-ion Battery. *J. Inorg. Mater.* **2020**, *35*, 134.
2. Marques, O.J.B.J.; Walter, M.D.; Timofeeva, E.V.; Segre, C.U. Effect of Initial Structure on Performance of High-Entropy Oxide Anodes for Li-Ion Batteries. *Batteries* **2023**, *9*, 115. [CrossRef]
3. Cao, K.; Jin, T.; Yang, L.; Jiao, L. Recent progress in conversion reaction metal oxide anodes for Li-ion batteries. *Mater. Chem. Front.* **2017**, *1*, 2213–2242. [CrossRef]

4. Rahman, M.M.; Marwani, H.M.; Algethami, F.K.; Asiri, A.M. Comparative performance of hydrazine sensors developed with Mn_3O_4/carbon-nanotubes, Mn_3O_4/graphene-oxides and Mn_3O_4/carbon-black nanocomposites. *Mater. Express* **2017**, *7*, 169–179. [CrossRef]

5. Xu, L.; Chen, X.; Zeng, L.; Liu, R.; Zheng, C.; Qian, Q.; Chen, Q. Synthesis of hierarchical Mn_3O_4 microsphere composed of ultrathin nanosheets and its excellent long-term cycling performance for lithium-ion batteries. *J. Mater. Sci. Mater. Electron.* **2019**, *30*, 3055–3060. [CrossRef]

6. Huang, H.; Zhao, Z.; Hu, W.; Liu, C.; Wang, X.; Zhao, Z.; Ye, W. Microwave-assisted hydrothermal synthesis of Mn3O4/reduced graphene oxide composites for efficiently catalytic reduction of 4-nitrophenol in wastewater. *J. Taiwan Inst. Chem. Eng.* **2018**, *84*, 101–109. [CrossRef]

7. Zhang, X.; Li, S.; Wang, S.; Wang, Z.; Wen, Z.; Ji, S.; Sun, J. An amorphous hierarchical MnO_2/acetylene black composite with boosted rate performance as an anode for lithium-ion batteries. *Dalton Trans.* **2021**, *50*, 10749–10757. [CrossRef] [PubMed]

8. Wu, L.L.; Zhao, D.L.; Cheng, X.W.; Ding, Z.W.; Hu, T.; Meng, S. Nanorod Mn_3O_4 anchored on graphene nanosheet as anode of lithium ion batteries with enhanced reversible capacity and cyclic performance. *J. Alloys Compd.* **2017**, *728*, 383–390. [CrossRef]

9. Wang, B.; Li, F.; Wang, X.; Wang, G.; Wang, H.; Bai, J. Mn_3O_4 nanotubes encapsulated by porous graphene sheets with enhanced electrochemical properties for lithium/sodium-ion batteries. *Chem. Eng. J.* **2019**, *364*, 57–69. [CrossRef]

10. Varghese, S.P.; Babu, B.; Prasannachandran, R.; Antony, R.; Shaijumon, M.M. Enhanced electrochemical properties of Mn_3O_4/graphene nanocomposite as efficient anode material for lithium ion batteries. *J. Alloys Compd.* **2019**, *780*, 588–596. [CrossRef]

11. Peng, H.-J.; Hao, G.-X.; Chu, Z.-H.; Lin, J.; Lin, X.-M.; Cai, Y.-P. Mesoporous Mn_3O_4/C Microspheres Fabricated from MOF Template as Advanced Lithium-Ion Battery Anode. *Cryst. Growth Des.* **2017**, *17*, 5881–5886. [CrossRef]

12. Gangaraju, D.; Sridhar, V.; Lee, I.; Park, H. Graphene—Carbon nanotube—Mn_3O_4 mesoporous nano-alloys as high capacity anodes for lithium-ion batteries. *J. Alloys Compd.* **2017**, *699*, 106–111. [CrossRef]

13. Deng, Y.; Wan, L.; Xie, Y.; Qin, X.; Chen, G. Recent advances in Mn-based oxides as anode materials for lithium ion batteries. *RSC Adv.* **2014**, *4*, 23914–23935. [CrossRef]

14. Fang, H.; Zou, W.; Yan, J.; Xing, Y.; Zhang, S. Facile Fabrication of Fe_2O_3 Nanoparticles Anchored on Carbon Nanotubes as High-Performance Anode for Lithium-Ion Batteries. *ChemElectroChem* **2018**, *5*, 2458–2463. [CrossRef]

15. Kuila, B.K.; Zaeem, S.M.; Daripa, S.; Kaushik, K.; Gupta, S.K.; Das, S. Mesoporous Mn_3O_4 coated reduced graphene oxide for high-performance supercapacitor applications. *Mater. Res. Express* **2018**, *6*, 015037–015046. [CrossRef]

16. Rosaiah, P.; Zhu, J.; Shaik, D.P.; Hussain, O.M.; Qiu, Y.; Zhao, L. Reduced graphene oxide/Mn_3O_4 nanocomposite electrodes with enhanced electrochemical performance for energy storage applications. *J. Electroanal. Chem.* **2017**, *794*, 78–85.

17. Zhou, Y.; Guo, L.; Shi, W.; Zou, X.; Xiang, B.; Xing, S. Rapid Production of Mn_3O_4/rGO as an Efficient Electrode Material for Supercapacitor by Flame Plasma. *Materials* **2018**, *11*, 881. [CrossRef]

18. Li, X.; Yue, W.; Li, W.; Zhao, J.; Zhang, Y.; Gao, Y.; Gao, N.; Feng, D.; Wu, B.; Wang, B. Rational design of 3D net-like carbon based Mn_3O_4 anode materials with enhanced lithium storage performance. *New J. Chem.* **2022**, *46*, 13220–13227. [CrossRef]

19. Cao, K. Mn_3O_4 nanoparticles anchored on carbon nanotubes as anode material with enhanced lithium storage. *J. Alloys Compd. Interdiscip. J. Mater. Sci. Solid-State Chem. Phys.* **2021**, *854*, 157176–157179. [CrossRef]

20. Seong, C.-Y.; Park, S.-K.; Bae, Y.; Yoo, S.; Piao, Y. An acid-treated reduced graphene oxide/Mn_3O_4 nanorod nanocomposite as an enhanced anode material for lithium ion batteries. *RSC Adv.* **2017**, *7*, 37502–37507. [CrossRef]

21. Yao, J.; Yue, J.L.; Guo, Q.; Xia, Q.; Hui, X. Highly Porous Mn_3O_4 Micro/Nanocuboids with In Situ Coated Carbon as Advanced Anode Material for Lithium-Ion Batteries. *Small* **2018**, *14*, 1704296.

22. Shah, H.U.; Wang, F.; Javed, M.S.; Shaheen, N.; Saleem, M.; Li, Y. Hydrothermal synthesis of reduced graphene oxide-Mn_3O_4 nanocomposite as an efficient electrode materials for supercapacitors. *Ceram. Int.* **2017**, *44*, 3580–3584. [CrossRef]

23. Alfaruqi, M.H.; Gim, J.; Kim, S.; Song, J.; Duong, P.T.; Jo, J.; Baboo, J.P.; Xiu, Z.; Mathew, V.; Kim, J. One-Step Pyro-Synthesis of a Nanostructured Mn_3O_4/C Electrode with Long Cycle Stability for Rechargeable Lithium-Ion Batteries. *Chemistry* **2016**, *22*, 2039–2045. [CrossRef] [PubMed]

24. Jing, M.; Hou, H.; Yang, Y.; Zhang, Y.; Yang, X.; Chen, Q.; Ji, X. Electrochemically Alternating Voltage Induced Mn_3O_4/Graphite Powder Composite with Enhanced Electrochemical Performances for Lithium-ion Batteries. *Electrochim. Acta* **2015**, *155*, 157–163. [CrossRef]

25. Yang, Z.; Lu, D.; Zhao, R.; Gao, A.; Chen, H. Synthesis of a novel structured Mn_3O_4@C composite and its performance as anode for lithium ion battery. *Mater. Lett.* **2017**, *198*, 97–100. [CrossRef]

26. Guo, W.; Wang, Y.; Li, Q.; Wang, D.; Zhang, F.; Yang, Y.; Yu, Y. SnO_2@C@VO_2 Composite Hollow Nanospheres as an Anode Material for Lithium-Ion Batteries. *ACS Appl. Mater. Interfaces* **2018**, *10*, 14993–14998. [CrossRef]

27. Thauer, E.; Shi, X.; Zhang, S.; Chen, X.; Deeg, L.; Wenelska, K.; Mijowska, E.; Lund, H.; Kaiser, M.J. Mn_3O_4 encapsulated in hollow carbon spheres coated by graphene layer for enhanced magnetization and lithium-ion batteries performance. *Energy* **2021**, *217*, 119399–119420. [CrossRef]

28. Oloore, L.E.; Gondal, M.A.; Popoola, A.; Popoola, I.K. Pseudocapacitive contributions to enhanced electrochemical energy storage in hybrid perovskite-nickel oxide nanoparticles composites electrodes. *Electrochim. Acta* **2020**, *361*, 137082–137091. [CrossRef]

29. Peng, L.; Hao, Q.; Xia, X.; Wu, L.; Xin, W. Hollow Amorphous $MnSnO_3$ Nanohybrid with Nitrogen-Doped Graphene for High-Performance Lithium Storage. *Electrochim. Acta* **2016**, *214*, 1–10.

30. Wang, Y.; Rao, S.; Mao, P.; Zhang, F.; Xiao, P.; Peng, L.; Zhu, Q. Controlled synthesis of Fe_3O_4@C@manganese oxides (MnO_2, Mn_3O_4 and MnO) hierarchical hollow nanospheres and their superior lithium storage properties. *Electrochim. Acta* **2020**, *337*, 135739–135777. [CrossRef]

31. Yan, D.-J.; Zhu, X.-D.; Mao, Y.-C.; Qiu, S.-Y.; Gu, L.-L.; Feng, Y.-J.; Sun, K.-N. Hierarchically organized CNT@TiO_2@Mn_3O_4 nanostructures for enhanced lithium storage performance. *J. Mater. Chem. A* **2017**, *5*, 17048–17055. [CrossRef]

32. Gao, D.D.; Luo, S.S.; Zhang, Y.H.; Liu, J.Y.; Wu, H.M.; Wang, S.Q.; He, P.X. Mn_3O_4/carbon nanotubes nanocomposites as improved anode materials for lithium-ion batteries. *J. Solid State Electrochem.* **2018**, *22*, 3409–3417. [CrossRef]

33. Liu, P.; Xia, X.; Lei, W.; Hao, Q. Rational synthesis of highly uniform hollow core–shell Mn_3O_4/CuO@TiO_2 submicroboxes for enhanced lithium storage performance. *Chem. Eng. J.* **2017**, *316*, 214–224. [CrossRef]

34. Zhu, S.; Li, J.; Deng, X.; He, C.; Liu, E.; He, F.; Shi, C.; Zhao, N. Ultrathin-Nanosheet-Induced Synthesis of 3D Transition Metal Oxides Networks for Lithium Ion Battery Anodes. *Adv. Funct. Mater.* **2017**, *27*, 1605017. [CrossRef]

35. Sun, X.; Si, W.; Liu, X.; Deng, J.; Schmidt, O.G. Multifunctional ni/nio hybrid nanomembranes as anode materials for high-rate li-ion batteries. *Nano Energy* **2014**, *9*, 168–175. [CrossRef]

36. Zhao, Y.; Ma, C.; Li, Y. One-step microwave preparation of a Mn_3O_4 nanoparticles/exfoliated graphite composite as superior anode materials for Li-ion batteries. *Chem. Phys. Lett.* **2017**, *673*, 19–23. [CrossRef]

37. Wang, Z.-H.; Yuan, L.-X.; Shao, Q.-G.; Huang, F.; Huang, Y.-H. Mn_3O_4 nanocrystals anchored on multi-walled carbon nanotubes as high-performance anode materials for lithium-ion batteries. *Mater. Lett.* **2012**, *80*, 110–113. [CrossRef]

38. Gan, Z.; Yin, J.; Xu, X.; Cheng, Y.; Yu, T. Nanostructure and Advanced Energy Storage: Elaborate Material Designs Lead to High-Rate Pseudocapacitive Ion Storage. *ACS Nano* **2022**, *16*, 5131–5152. [CrossRef]

39. Xiong, P.; Ma, R.; Sakai, N.; Sasaki, T. Genuine Unilamellar Metal Oxide Nanosheets Confined in a Superlattice-like Structure for Superior Energy Storage. *ACS Nano* **2018**, *12*, 1768–1777. [CrossRef]

40. Yoon, E.S.; Choi, B.G.; Jeon, H.J. Highly ordered nanoscale phosphomolybdate-grafted polyaniline/metal hybrid layered structures prepared via secondary sputtering phenomenon as high-performance pseudocapacitor electrodes. *Phys. Scr.* **2021**, *96*, 125882. [CrossRef]

41. Meng, X.; Guan, Z.; Zhao, J.; Cai, Z.; Li, S.; Bian, L.; Song, Y.; Guo, D.; Liu, X. Lithium-pre-intercalated T-Nb2O5/graphene composite promoting pseudocapacitive performance for ultralong lifespan capacitors. *Chem. Eng. J.* **2022**, *43*, 438–446. [CrossRef]

42. Chu, Y.; Guo, L.; Xi, B.; Feng, Z.; Wu, F.; Lin, Y.; Liu, J.; Sun, D.; Feng, J.; Qian, Y.; et al. Embedding MnO@Mn_3O_4 Nanoparticles in an N-Doped-Carbon Framework Derived from Mn-Organic Clusters for Efficient Lithium Storage. *Adv. Mater.* **2018**, *30*, 1704244. [CrossRef] [PubMed]

43. Avvaru, V.S.; Fernandez, I.J.; Feng, W.; Hinder, S.J.; Rodríguez, M.C.; Etacheri, V. Extremely pseudocapacitive interface engineered CoO@3D-NRGO hybrid anodes for high energy/power density and ultralong life lithium-ion batteries. *Carbon* **2021**, *171*, 869–881. [CrossRef]

44. Vincent, M.; Avvaru, V.S.; Rodriguez, M.C.; Haranczyk, M.; Etacheri, V. High-rate and ultralong-life Mg-Li hybrid batteries based on highly pseudocapacitive dual-phase TiO_2 nanosheet cathodes. *J. Power Sources* **2021**, *15*, 506. [CrossRef]

45. Wang, X. Facile synthesis of Mn_3O_4 hollow polyhedron wrapped by multiwalled carbon nanotubes as a high-efficiency microwave absorber. *Ceram. Int.* **2020**, *46*, 6550–6559. [CrossRef]

46. Choudhury, B.J.; Roy, K.; Moholkar, V.S. Improvement of Supercapacitor Performance through Enhanced Interfacial Interactions Induced by Sonication. *Ind. Eng. Chem. Res.* **2021**, *60*, 7611–7623. [CrossRef]

47. Bhagwan, J.; Sahoo, A.; Yadav, K.L.; Sharma, Y. Porous, one dimensional and High Aspect Ratio Mn_3O_4 Nanofibers: Fabrication and Optimization for Enhanced Supercapacitive Properties. *Electrochim. Acta* **2015**, *174*, 992–1001. [CrossRef]

48. Wang, J.G.; Jin, D.; Zhou, R.; Li, X.; Liu, X.R.; Shen, C.; Xie, K.; Li, B.; Kang, F.; Wei, B. Highly flexible graphene/Mn_3O_4 nanocomposite membrane as advanced anodes for li-ion batteries. *Acs Nano* **2016**, *10*, 6227–6234. [CrossRef]

49. Dong, S.; Chang, C.; Liang, Z.; Zhang, Z.; An, L. Electroless deposition of carbon nanotubes doped with nickel and their electrical contact properties. *J. Xian Univ.* **2020**, *47*, 88–94.

50. Zhang, J.; Chu, R.X.; Chen, Y.L.; Zeng, Y.; Zhang, Y.; Guo, H. Porous carbon encapsulated Mn_3O_4 for stable lithium storage and its ex-situ XPS study. *Electrochim. Acta* **2019**, *319*, 518–526. [CrossRef]